Simulation of ionospheric disturbances created by Alfvén waves

D. Sydorenko[1] and R. Rankin[1]

Received 5 March 2012; revised 9 August 2012; accepted 10 August 2012; published 29 September 2012.

[1] A two-dimensional numerical model of low-altitude auroral flux tubes has been developed for simulation of coupling between the magnetosphere and the ionosphere. The model considers a realistic ionosphere with multiple ion and neutral species, collisions, cooling and heating processes, as well as the North-South electric field due to the global azimuthal plasma convection. In the paper, a detailed description of the model is given. A representative simulation where the ionosphere is perturbed by an Alfvén wave is discussed. The model demonstrates formation of intense parallel electric fields, radiation of Alfvén waves by density perturbations in the convective flow, and electron and ion heating.

Citation: Sydorenko, D., and R. Rankin (2012), Simulation of ionospheric disturbances created by Alfvén waves, *J. Geophys. Res.*, *117*, A09229, doi:10.1029/2012JA017693.

1. Introduction

[2] Simulation of coupling between the magnetosphere and ionosphere (MI-coupling) requires an adequate ionospheric model. A frequently used method is to describe the electrodynamic properties of the ionosphere by height integrated conductivities [e.g., *Lysak*, 1991; *Streltsov and Lotko*, 2004]. In such an approach, the ionosphere is an infinitely thin layer and altitude variations of ionospheric parameters are omitted. Another way is to solve dynamic equations for the ionospheric plasma while resolving the vertical structure of the ionosphere. This method is more correct but also much more complex. Not surprisingly, although there are many detailed ionospheric models [*Schunk*, 1996], the number of codes for simulation of MI coupling that include a realistic ionosphere is relatively small. A review of several such models is given below.

[3] *Lysak* [1997] described wave propagation through the ionosphere in the linear approximation, including Hall and Pedersen conductivities, which were given realistic functions of altitude and did not change with time. He demonstrated that reflection of a shear Alfvén wave from the ionosphere is accompanied by excitation of a compressional Alfvén wave propagating transversely to the geomagnetic field. *Noël et al.* [2000] created an ionospheric model where the electrostatic field was calculated from Ohm's law and the quasineutrality condition. This model was used to demonstrate the formation of sharp gradients during auroral precipitation. Later, *Noël et al.* [2005] applied this model to study wave heating of the ionosphere, although the wave propagation itself was not considered, due to limitations of the electrostatic model. *Zhu et al.* [2001] developed a model capable of describing interaction between an Alfvén wave perturbation and a height-resolved ionosphere. This model considered a plasma consisting of electrons, a single species of ions, and a single species of neutrals. The model demonstrated heating of ionospheric electrons and ions by the wave and particle precipitation. *Zhu et al.* [2001] used cartesian coordinates. Recently, *de Boer et al.* [2010] developed a model of the high-latitude ionosphere which used a non-structured triangular mesh and accounted for inclination of the geomagnetic field. The electrostatic field was calculated from the condition of quasineutrality, similar to *Noël et al.* [2000]. The model demonstrated that a high-density plasma column created by electron precipitation is distorted by the vertical shear of the horizontal ion flow in the E-layer. The models above are two-dimensional. *Wang et al.* [2004] reported a three-dimensional model of the coupled global magnetosphere and ionosphere. This model has relatively coarse resolution in the ionosphere (few degrees in latitude and longitude) which can be improved locally by means of nested grids. A test simulation described in the paper showed that the temperature of the neutral atmosphere increases due to friction between neutrals and convecting ions, which increases atmospheric density at higher altitudes.

[4] *Sydorenko et al.* [2010] developed a two-dimensional model of the ionospheric Alfvén resonator (IAR) with a perfectly conducting ionosphere. The present paper is devoted to the description of a new model, where the IAR model of *Sydorenko et al.* [2010] is combined self-consistently with a realistic model of the ionosphere based on *Schunk* [1988, hereinafter S88]. In contrast to electrostatic models of *Noël et al.* [2000] and *de Boer et al.* [2010], the new model includes Alfvén waves. Compared to the model of *Zhu et al.* [2001], the new model considers multiple ion species and uses a more realistic dipole geometry.

[5] The paper is organized as follows. In Section 2, the description of the ionospheric model is given. Section 3 discusses a representative simulation, where an Alfvén wave incident from the magnetosphere is reflected from the ionosphere. A summary of the simulation results and a discussion

[1]Department of Physics, University of Alberta, Edmonton, Alberta, Canada.

Corresponding author: D. Sydorenko, Department of Physics, University of Alberta, 4-183 CCIS, Edmonton, AB T6G 2E1, Canada. (sydorenk@ualberta.ca)

0148-0227/12/2012JA017693

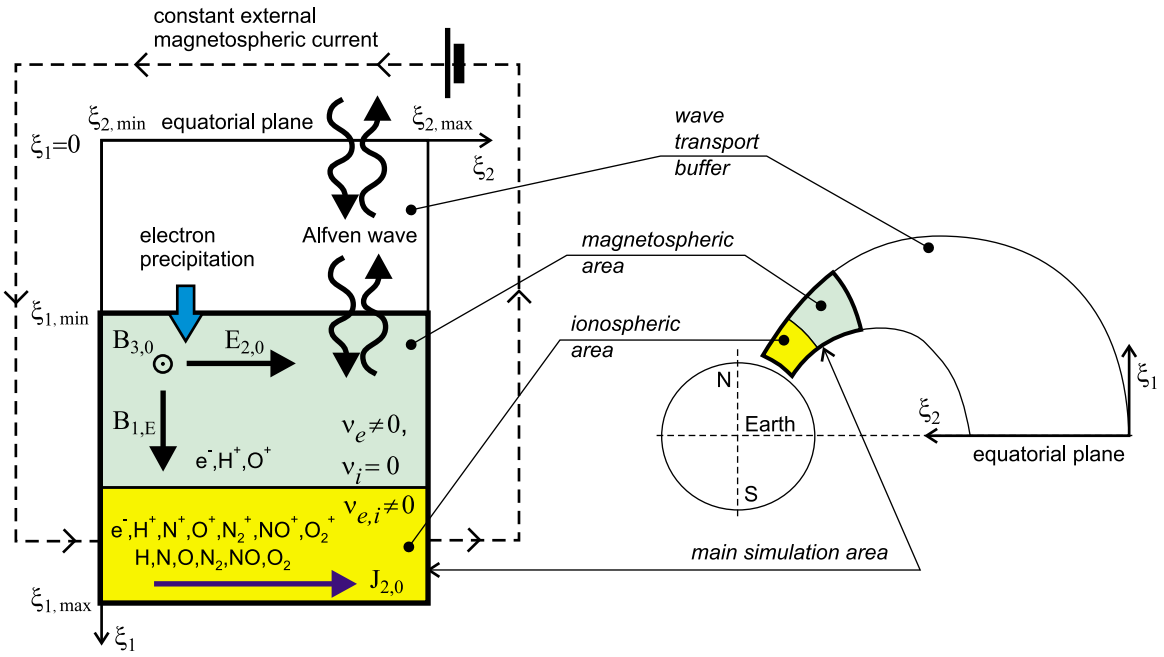

Figure 1. Schematic of the simulated ionosphere-magnetosphere system in dipole coordinates (left) and real space (right, dimensions are approximate). In the real space schematic, line *NS* is the geomagnetic dipole axis passing through the north (*N*) and south (*S*) magnetic poles, the equatorial plane is perpendicular to the dipole axis rather than the Earth rotation axis, the dipole coordinate axes ξ_1 and ξ_2 are shown for a point in the equatorial plane.

of possible improvements of the model is presented in Section 4. The boundary conditions are explained in Appendix A. Features of the numerical grid are discussed in Appendix B. Finally, calculation of the initial state can be found in Appendix C.

2. Numerical Model of the Ionosphere

[6] The model of the near-Earth plasma described in the present paper considers a two-dimensional area in the meridional plane bounded by dipole geomagnetic field lines from the northern and southern sides (see the real space schematic in the right-hand side of Figure 1). Dipole coordinates are used and azimuthal symmetry is assumed. A schematic of the simulation area in the dipole coordinate space is shown in the left-hand side of Figure 1. The yellow box in the bottom of this schematic denotes a layer of collisional plasma with multiple ion (H^+, N^+, O^+, N_2^+, NO^+, O_2^+) and neutral (H, N, O, N_2, NO, O_2) components. This layer represents the ionosphere, it is well resolved by the numerical grid.

[7] The ionosphere can be perturbed by an Alfvén wave or electron precipitation; the former is calculated self-consistently while the latter is included as a parametric model. The details of the precipitation model and simulation of ionospheric perturbations created by precipitation are out of the scope of the present paper and will be described in a future publication. Alfvén waves are injected into the system through the top side of the simulation area.

[8] Above the ionosphere, the plasma contains H^+ and O^+ ion species (the blue box in Figure 1, referred to as the magnetospheric area henceforward). In the magnetospheric area, the neutrals are omitted, the ion motion is collisionless while the electrons are still affected by Coulomb collisions with the ions. Note that the typical thickness of the ionospheric layer is about one thousand kilometers, which ensures that collisions with neutrals are insignificant at the top of the ionospheric layer and transition to the magnetospheric area is smooth.

[9] Initially, a convection electric field directed across the geomagnetic field (in the North–South direction) is applied to represent the electric field of azimuthal plasma convection. The corresponding global parallel electric currents and the generator area in the magnetosphere are not a part of the simulated system and are shown in the left-hand side schematic in Figure 1 as an external circuit for the sake of completeness only. It is assumed that processes inside the simulation area do not affect the global current system. This assumption allows to consider electromagnetic fields along the boundary geomagnetic field lines constant in time.

[10] The ionospheric and the magnetospheric areas together form the main simulation area (bordered by the bold black line in Figure 1). Electromagnetic equations solved in the main area are two-dimensional and constitute most of the numerical cost. Above the main area there is a region which stretches up to the equatorial plane (the white box in Figure 1). Hereafter, the area between the equatorial plane and the top boundary of the main simulation area is called the wave transport buffer. Equations solved inside the buffer are simplified and the related numerical cost is minimal. The main role of this buffer is to provide boundary conditions at the top of the main simulation area. It is necessary to mention that the Alfvén wave is specified at the equatorial plane and travels through the wave transport buffer before entering

the main area. Detailed description of the wave transport buffer is given in Appendix A.

[11] Compared to the base IAR model of *Sydorenko et al.* [2010], significant changes have been made in the electromagnetic solver, boundary conditions, initial conditions, and configuration of the numerical grid. The purpose of these modifications is to ensure correct and cost-effective simulation of perturbations with small transverse spatial scales in the ionosphere.

[12] Before proceeding, it is useful to define dipole coordinates $\xi_{1,2,3}$ as follows: $\xi_1 = \cos\vartheta/r^2$, $\xi_2 = \sin^2\vartheta/r$, and $\xi_3 = -\varphi$, where $\{r, \vartheta, \varphi\}$ are the ordinary spherical coordinates. The dipole metric factors $h_{1,2,3}$ are $h_2 = r^2/\left(\sin\vartheta\sqrt{1+3\cos^2\vartheta}\right)$, $h_3 = r\sin\vartheta$, and $h_1 = h_2h_3$. In the present paper, vector components along the geomagnetic field have subscript 1, vector components perpendicular to the geomagnetic field in the meridional plane have subscript 2, and azimuthal vector components have subscript 3. Below, vectors along the ξ_1 direction are referred to as the parallel ones, whereas vectors along the ξ_2 direction are referred to as the transverse ones.

2.1. Electromagnetic Field Equations

[13] The electromagnetic field components E_1, E_2, and B_3 are defined by the following set of equations involving the electric current density components J_1 and J_2:

$$\frac{1}{c^2}\frac{\partial E_2}{\partial t} = -\frac{1}{h_1h_3}\frac{\partial h_3B_3}{\partial \xi_1} - \mu_0 J_2, \tag{1}$$

$$\frac{\partial B_3}{\partial t} = \frac{1}{h_1h_2}\left(\frac{\partial h_1E_1}{\partial \xi_2} - \frac{\partial h_2E_2}{\partial \xi_1}\right), \tag{2}$$

$$E_1\sum_{\alpha=e,O^+,H^+}\frac{n_\alpha e^2}{m_\alpha} = \sum_{\alpha=e,O^+,H^+} q_\alpha\left\{\frac{1}{h_1}\frac{\partial}{\partial\xi_1}\left(\frac{p_\alpha}{m_\alpha}\right) + n_\alpha[(\mathbf{u}_\alpha\cdot\nabla)\mathbf{u}_\alpha]_1 - u_{\alpha,1}\frac{\partial n_\alpha}{\partial t}\right\} - \sum_{\alpha=O^+,H^+}\frac{n_\alpha e^2}{m_\alpha}u_{\alpha,2}B_3 + \frac{\partial J_1}{\partial t} - en_e\sum_{\alpha=O^+,H^+}\nu_{e,\alpha}\left(u_{e,1}-u_{\alpha,1}\right), \tag{3a}$$

$$E_1 = -\frac{1}{en_eh_1}\frac{\partial}{\partial\xi_1}p_e - \frac{m_e}{e}[(\mathbf{u}_e\cdot\nabla)\mathbf{u}_e]_1 + \frac{m_eu_{e,1}}{en_e}\frac{\partial n_e}{\partial t} + \frac{m_e}{n_ee^2}\frac{\partial J_1}{\partial t} + \frac{m_e}{e}g_1 - \frac{m_e\nu_eu_{e,1}}{e}, \tag{3b}$$

$$\frac{\partial}{\partial\xi_1}(J_1h_2h_3) + \frac{\partial}{\partial\xi_2}(J_2h_1h_3) = 0, \tag{4}$$

where c is the light speed, e is the elementary charge (positive), q_α, m_α, n_α, p_α, and $\mathbf{u}_\alpha$ are the charge, mass, number density, pressure, and vector velocity of species α, subscript $\alpha = e$ is for the electrons and $\alpha = H^+, N^+, O^+, N_2^+, NO^+, O_2^+$ is for the ion species, $q_e = -e$, $q_\alpha = e$ for the ions, $\nu_{e,\alpha}$ is the electron momentum transfer collision frequency for collisions between electrons and ions of species α, ν_e is the total electron momentum transfer collision frequency which includes collisions with both ions and neutrals, g_1 is the acceleration due to the gravity force along the geomagnetic field. The collision frequencies and the convection terms $(\mathbf{u}\cdot\nabla)\mathbf{u}$ are defined below.

[14] Equations (1) and (2) are the familiar Maxwell equations. It is important that in (1), the transverse current density J_2 contains Alfvén wave ion polarization current proportional to $\partial E_2/\partial t$, see the motion equations (7) and (15). Equations (3a) and (3b) define the parallel electric field in the magnetospheric and the ionospheric areas, respectively. These equations are obtained from the fluid motion equations for the plasma components specified below. Note that equation (3b) contains only electron terms because for simplicity it is assumed that inside the ionosphere the ions do not move along the geomagnetic field. The last term in the right-hand side (RHS) of (3a) and (3b) describes the part of the parallel electric field which maintains electric current through a collisional plasma.

[15] Equation (4) is the electric current continuity equation under the condition of plasma quasineutrality. The parallel electric current in the magnetospheric area is created by electrons and ions, $J_1 = J_{1,ext} + \sum_{\alpha=e,O^+,H^+} q_\alpha n_\alpha u_{\alpha,1}$. In the ionosphere, the current is due to electrons only, $J_1 = J_{1,ext} - en_eu_{e,1}$. Here $J_{1,ext}$ is the parallel electric current density due to auroral electron precipitation, while in the present paper $J_{1,ext} = 0$. The transverse electric current is created by ions, $J_2 = \sum_\alpha q_\alpha n_\alpha u_{\alpha,2}$, where summation involves H^+ and O^+ ions in the magnetospheric area and $H^+, N^+, O^+, N_2^+, NO^+$, and O_2^+ ions in the ionosphere.

[16] There is an obvious linear relation between the transverse current J_2 and the transverse electric field E_2, which can be straightforwardly obtained using the ion dynamics equations described in Sections 2.2 and 2.3. With this relation, equations (1)–(4) in finite difference form reduce to a system of linear equations for the advanced values B_3^{n+1} and E_1^{n+1} (superscript $n+1$ denotes values at the moment of time $t_{n+1} = t_n + \Delta t$, where Δt is the time step of the simulation). This system is solved using the successive over-relaxation method [e.g., *Young*, 1970].

[17] The model presented here does not use the Poisson's equation or the parallel component of the Maxwell-Ampere equation to find the parallel electric field. Instead, equation (4) ensures that the parallel plasma flows maintain plasma quasineutrality, while equations (3a) and (3b) provide the parallel electric field that supports the required flows. In a stationary state, $\nabla\times\mathbf{E} = 0$ according to equation (2), and therefore, the model ensures that the stationary electric field can be represented as $\mathbf{E} = -\nabla\Phi$, where Φ is the electrostatic potential. Since the electric current is directly related to the electric field via equations of plasma motion, equation (4) becomes an equation for Φ in the stationary state. The electric charge density creating this potential can be found from the Poisson's equation. Note that the assumption of quasineutrality can be used only if the difference between the ion and electron densities is much smaller than the plasma density itself. In most cases, including the low-amplitude Alfvén wave considered in the present paper, this is true. Examples of phenomena where the quasineutrality is strongly violated include the plasma sheath, double layers, shock waves, etc.

[18] The boundary conditions required to solve the electromagnetic field equations (1)–(4) are given in Appendix A.

2.2. Plasma Dynamics Inside the Magnetospheric Area

[19] Equations describing plasma dynamics in the magnetospheric area are mostly the same as in *Sydorenko et al.* [2010]. For ions ($\alpha = H^+, O^+$):

$$-\frac{\partial n_\alpha}{\partial t} = \frac{1}{h_1 h_2 h_3}\left[\frac{\partial\left(n_\alpha u_{\alpha,1} h_2 h_3\right)}{\partial \xi_1} + \frac{\partial\left(n_\alpha u_{\alpha,2} h_1 h_3\right)}{\partial \xi_2}\right], \quad (5)$$

$$\frac{\partial u_{\alpha,1}}{\partial t} = -\left[(\mathbf{u}_\alpha\cdot\nabla)\mathbf{u}_\alpha\right]_1 + \frac{e}{m_\alpha}\left(E_1 + u_{\alpha,2}B_3\right) - \frac{1}{m_\alpha n_\alpha h_1}\frac{\partial}{\partial \xi_1} n_\alpha T_\alpha + g_1, \quad (6)$$

$$u_{\alpha,2} = \frac{m_\alpha}{eB_E^2}\frac{\partial E_2}{\partial t}, \quad (7)$$

$$u_{\alpha,3} = -\frac{E_2}{B_E}, \quad (8)$$

where B_E is the geomagnetic field and the parallel component of the convective velocity derivative is

$$\left[(\mathbf{u}_\alpha\cdot\nabla)\mathbf{u}_\alpha\right]_1 = \frac{u_{\alpha,1}}{h_1}\frac{\partial u_{\alpha,1}}{\partial \xi_1} + \frac{u_{\alpha,2}}{h_2}\frac{\partial u_{\alpha,1}}{\partial \xi_2} + \frac{u_{\alpha,1}u_{\alpha,2}}{2h_1^2 h_2}\frac{\partial h_1^2}{\partial \xi_2} - \frac{u_{\alpha,2}^2}{2h_1 h_2^2}\frac{\partial h_2^2}{\partial \xi_1} - \frac{u_{\alpha,3}^2}{2h_1 h_3^2}\frac{\partial h_3^2}{\partial \xi_1}.$$

For electrons:

$$n_e = n_{O^+} + n_{H^+}, \quad (9)$$

$$\frac{\partial u_{e,1}}{\partial t} = -\left[(\mathbf{u}_e\cdot\nabla)\mathbf{u}_e\right]_1 - \frac{e}{m_e}E_1 - \frac{1}{m_e n_e h_1}\frac{\partial}{\partial \xi_1} n_e T_e + g_1 + \sum_{\alpha=H^+,O^+}\nu_{e,\alpha}\left(u_{\alpha,1} - u_{e,1}\right), \quad (10)$$

$$u_{e,2} = 0, \quad (11)$$

$$u_{e,3} = -\frac{E_2}{B_E}, \quad (12)$$

where the parallel component of the convective velocity derivative is

$$\left[(\mathbf{u}_e\cdot\nabla)\mathbf{u}_e\right]_1 = \frac{u_{e,1}}{h_1}\frac{\partial u_{e,1}}{\partial \xi_1} - \frac{u_{e,3}^2}{2h_1 h_3^2}\frac{\partial h_3^2}{\partial \xi_1}. \quad (13)$$

In the electron motion equation (10), the additional term due to the electron-ion collisions is introduced to ensure the continuity of electron dynamics across the interface between the ionospheric and magnetospheric areas. Since electrons in the ionospheric area collide with both ions and neutrals, the interface must be selected at sufficiently high altitude, where collisions with neutrals are far less important than the Coulomb collisions.

[20] Although electron collision processes are accounted for, the ion motion equations (6)–(8) are still collisionless for the following reasons. On one hand, as it is mentioned in the previous paragraph, the ion-neutral collisions are insignificant here because of the very low density of neutrals. On the other hand, the ion momentum transfer frequency due to the electron-ion collisions is also very low, $\nu_{\alpha,e} = (m_e/m_\alpha)\nu_{e,i}$, where $\nu_{e,i}$ is the total electron momentum transfer frequency due to Coulomb collisions with all ion species in the plasma.

[21] In the magnetospheric area, for the sake of simplicity, it is assumed that local values of temperatures T_α of all species do not change with time, i.e. $\partial T_\alpha/\partial t = 0$, where $\alpha = e, O^+, H^+$.

2.3. Plasma Dynamics Inside the Ionosphere

[22] Equations describing dynamics of ion species α ($\alpha = H^+, N^+, O^+, N_2^+, NO^+, O_2^+$) are:

$$u_{\alpha,1} = 0, \quad (14)$$

$$u_{\alpha,2} = \frac{1}{1+\nu_\alpha^2/\Omega_\alpha^2}\frac{m_\alpha}{eB_E^2}\left(\frac{\partial E_2}{\partial t} + \nu_\alpha E_2\right), \quad (15)$$

$$u_{\alpha,3} = -\frac{1}{1+\nu_\alpha^2/\Omega_\alpha^2}\frac{E_2}{B_E}, \quad (16)$$

$$\left(\frac{\partial}{\partial t} + \frac{u_{\alpha,2}}{h_2}\frac{\partial}{\partial \xi_2}\right) n_\alpha = -\frac{n_\alpha}{h_1 h_2 h_3}\frac{\partial}{\partial \xi_2} u_{\alpha,2} h_1 h_3 + P_\alpha, \quad (17)$$

$$\left(\frac{\partial}{\partial t} + \frac{u_{\alpha,2}}{h_2}\frac{\partial}{\partial \xi_2}\right) p_\alpha = -\frac{5}{3}\frac{p_\alpha}{h_1 h_2 h_3}\frac{\partial}{\partial \xi_2} u_{\alpha,2} h_1 h_3 + 2n_\alpha\sum_\beta \frac{m_\alpha \nu_{\alpha,\beta}}{m_\alpha + m_\beta}(T_n - T_i) + 2n_e\frac{m_e\nu_{e,\alpha}}{m_\alpha + m_e}(T_e - T_i) + \frac{2}{3}n_\alpha\sum_\beta\frac{m_\alpha m_\beta \nu_{\alpha,\beta}}{m_\alpha + m_\beta}\left(u_{\alpha,2}^2 + u_{\alpha,3}^2\right). \quad (18)$$

where $\Omega_\alpha = eB_E/m_\alpha$ is the ion cyclotron frequency.

[23] Equation (14) corresponds to the simplifying assumption that the ions do not move along the geomagnetic field. Since the parallel ion motion is permitted in the magnetospheric area, $u_{\alpha,1}$ is discontinuous at the interface between the ionospheric and the magnetospheric areas. In order to minimize possible negative effects of this discontinuity, simulations with the present model must be carried out in a regime when the parallel ion flows above the ionosphere are much slower than the electron flow. In the representative simulation described in Section 3, for example, the amplitude of the parallel electron flow velocity above the ionosphere reaches about 20 km/s while for H^+ it is about 8 m/s and for O^+ ions it is only 2 m/s. The parallel ion dynamics in the ionosphere will be added in the future versions of the model.

[24] The first and the last terms in the RHS of (15) correspond to the ion polarization current of an Alfvén wave and the Pedersen current, respectively. Equation (15) ensures a smooth transition of transverse electric current from lower altitudes, where it is mostly the Pedersen current, to higher altitudes, where the ion polarization current of the Alfvén

wave is dominant. It is instructive to introduce an "Alfvén" conductivity $\sigma_A = \omega/\mu_0 V_A^2$, where ω is the wave frequency and $V_A = B_E \Big/ \left(\mu_0 \sum_\alpha m_\alpha n_\alpha\right)^{1/2}$ is the Alfvén speed, summation is over the ion species. The amplitude of the wave ion polarization current is then $J_{2,A} = \sigma_A E_{2,A}$, where $E_{2,A}$ is the Alfvén wave transverse electric field amplitude. The Pedersen conductivity is $\sigma_P = \sum_\alpha \sigma_{P\alpha}$, where summation is over the ion species and

$$\sigma_{P\alpha} = \frac{\nu_\alpha/\Omega_\alpha}{1+\nu_\alpha^2/\Omega_\alpha^2}\frac{en_\alpha}{B_E}.$$

Comparison of the Pedersen conductivity (solid black curve in Figure 3b) with the "Alfvén" conductivity (dashed green curve in Figure 3b) shows that for the selected ionospheric and wave parameters, a transition between the two regimes occurs at an altitude about 300 km.

[25] Effects of Hall currents are omitted in the present model (see the discussion in the concluding section). The total ion momentum transfer collision frequency ν_α in (15) and (16) is the combined frequency of collisions with neutrals: $\nu_\alpha = \sum_\beta \nu_{\alpha,\beta}$ where subscript $\beta = H, N, O, N_2, O_2$ labels the neutral species. The individual frequencies of collision $\nu_{\alpha,\beta}$ between ion species α and neutral species β include resonant and non-resonant ion-neutral interactions and are given by Tables 3, 4, and equation (9) of S88.

[26] In the continuity equation (17), the term P_α describes combined production and loss due to ionization by electron precipitation and chemical reactions. In the present paper $P_\alpha = 0$.

[27] The ion pressure equation (18) is the simplified version of equation (3) of S88. The second term in the RHS of (18) describes heat exchange between ions and neutrals, the summation is over neutral species β. The third term in the RHS of (18) describes heat exchange with electrons. The electron-ion collision frequency $\nu_{e,\alpha}$ for ion species α is given by equation (7) of S88 with density n_α. The last term in the RHS of (18) describes frictional ion heating due to collisions with neutrals. Collision frequencies $\nu_{\alpha,\beta}$ are the same as the ones described above for equations (15) and (16).

[28] The densities n_α and pressures p_α of each ion species are advanced separately. Therefore, in general, each ion species should have a different temperature $T_\alpha = p_\alpha/n_\alpha$. It is commonly accepted that the differences in temperatures of ion species in the ionosphere can be neglected [*Schunk*, 1996]. One way to implement this assumption is to derive an equation for the common ion temperature from (18), as in S88. Another way is to solve the pressure equation for one major ion species, find its temperature, and then use it as the common ion temperature [*Kirchengast*, 1996]. In the present model, the following procedure is introduced. At each time step, once all n_α are updated with (17) and p_α are updated with (18), the common ion temperature is calculated as $T_i = \sum_\alpha p_\alpha \Big/ \sum_\alpha n_\alpha$. Then, for each species, the updated p_α is set equal to $n_\alpha T_i$. This procedure allows use of the same semi-Lagrangian algorithm [*Staniforth and Cote*, 1991] for calculation of n_α and p_α. It does not change the total thermal energy and accounts for contributions of minor ion species that otherwise cause "wandering" of the pressures of these species.

[29] The electron dynamic equations are:

$$\frac{\partial u_{e,1}}{\partial t} = -[(\mathbf{u}_e\cdot\nabla)\mathbf{u}_e]_1 - \frac{e}{m_e}E_1 - \frac{1}{m_e n_e h_1}\frac{\partial}{\partial\xi_1}n_e T_e + g_1 - \nu_e u_{e,1}, \tag{19}$$

$$u_{e,2} = 0, \tag{20}$$

$$u_{e,3} = -\frac{E_2}{B_E}, \tag{21}$$

$$n_e = n_{H^+} + n_{N^+} + n_{O^+} + n_{N_2^+} + n_{NO^+} + n_{O_2^+}, \tag{22}$$

$$\begin{aligned}\left(\frac{\partial}{\partial t} + \frac{u_{e,1}}{h_1}\frac{\partial}{\partial\xi_1}\right)p_e = &-\frac{5}{3}\frac{p_e}{h_1h_2h_3}\frac{\partial}{\partial\xi_1}u_{e,1}h_2h_3 \\ &-\frac{2}{3h_1h_2h_3}\frac{\partial}{\partial\xi_1}q_1h_2h_3 \\ &-2n_e\sum_\alpha\frac{m_e\nu_{e,\alpha}}{m_\alpha+m_e}(T_e-T_i) \\ &+\frac{2}{3}n_e\sum_\alpha\frac{m_em_\alpha\nu_{e,\alpha}}{m_e+m_\alpha}\left[u_{e,1}^2+u_{\alpha,2}^2\right. \\ &\left.+(u_{e,3}-u_{\alpha,3})^2\right]+\frac{2}{3}n_e\sum_\beta\frac{m_em_\beta\nu_{e,\beta}}{m_e+m_\beta} \\ &\cdot\left(u_{e,1}^2+u_{e,3}^2\right)+\frac{2}{3}\left(Q_e^{precip}-C_e\right).\end{aligned} \tag{23}$$

[30] In the parallel electron motion equation (19), the convection term is given by (13), the total electron momentum transfer collision frequency is $\nu_e = \sum_\alpha \nu_{e,\alpha} + \sum_\beta \nu_{e,\beta}$, where $\nu_{e,\alpha}$ is defined above, $\nu_{e,\beta}$ is the electron momentum transfer frequency for collisions with neutrals of species β [Table 1 of S88], the summation over neutral species includes $\beta = H, O, N_2, O_2$. In the magnetospheric area, the total electron momentum transfer frequency is $\nu_e = \sum_\alpha \nu_{e,\alpha}$. The total frequency ν_e is approximately continuous across the interface between the ionospheric and magnetospheric areas (see curve formed by crosses in Figure 2d). In a stationary state, if the electron pressure gradients, gravity, and the nonlinear effects are negligible, equation (19) provides a useful relation between the parallel electric current density and field: $J_1 = \sigma_0 E_1$ where $\sigma_0 = n_e e^2/m_e\nu_e$ is the parallel conductivity. The parallel conductivity saturates at higher altitudes (see the dash-dot red curve in Figure 3b) because the frequency of electron-ion collisions is proportional to the plasma density.

[31] The electron motion in the transverse (meridional) direction is omitted, as in Section 2.3 (compare equations (20) and (11)). The azimuthal motion of electrons is defined by equation (21), which is the same as equation (12) in the magnetospheric area because the electron cyclotron frequency significantly exceeds the electron momentum transfer

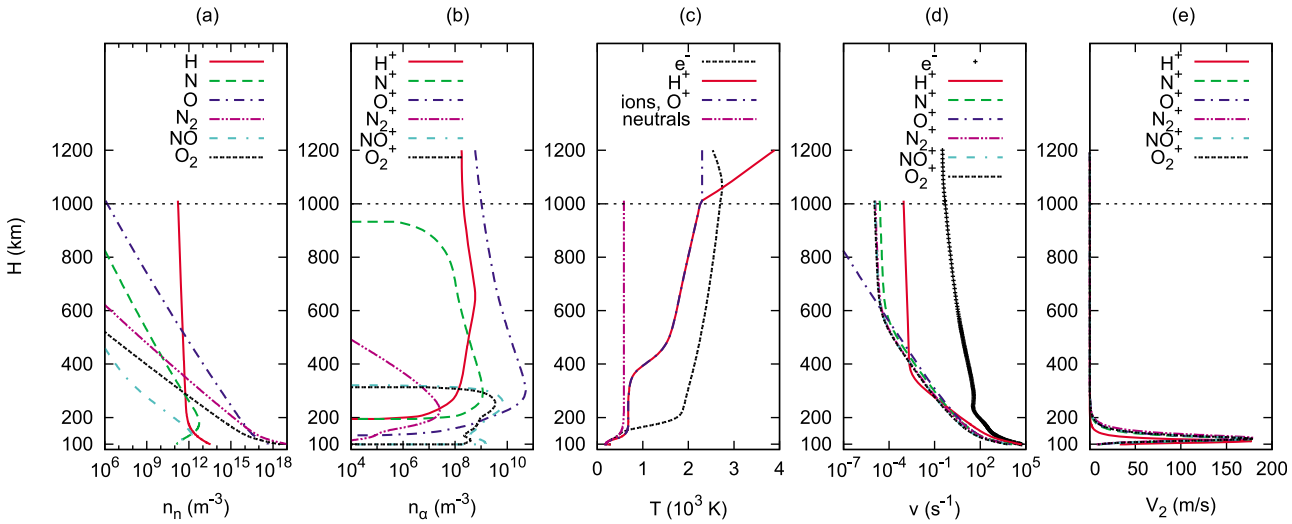

Figure 2. Initial profiles of number densities of (a) neutrals and (b) ions, (c) temperatures, (d) collision frequencies, and (e) transverse ion flow velocities obtained along the middle geomagnetic field line. Everywhere, the vertical axis is the altitude. Horizontal dashed lines mark the top ionospheric boundary at 1000 km. The bottom boundary is at 100 km.

frequency. Equation (22) sets the electron density value according to the quasineutrality assumption.

[32] The second term in the RHS of the electron pressure equation (23) contains the electron heat flow in the parallel direction [cf. S88, equations (64), (66), and (67)]

$$q_1 = \frac{5}{2} p_e u_{e,1} - \frac{5 p_e}{2 m_e \nu_e h_1} \frac{\partial}{\partial \xi_1} T_e,$$

where the electron momentum transfer frequency ν_e is the same as the one used in the parallel electron motion equation (19) above. The third term in the RHS of (23) describes heat exchange with ions, the summation is over ion species α. The fourth term in the RHS of (23) describes frictional electron heating due to collisions with ions, the summation is over ion species α. The fifth term in the RHS of (23) describes frictional electron heating due to collisions with neutrals, the summation is over neutral species β. The term Q_e^{precip} in equation (23) describes electron heating due to precipitation of energetic electrons. In the present paper $Q_e^{precip} = 0$. The term C_e describes electron cooling due to excitation of vibrational and rotational levels of N_2 and O_2

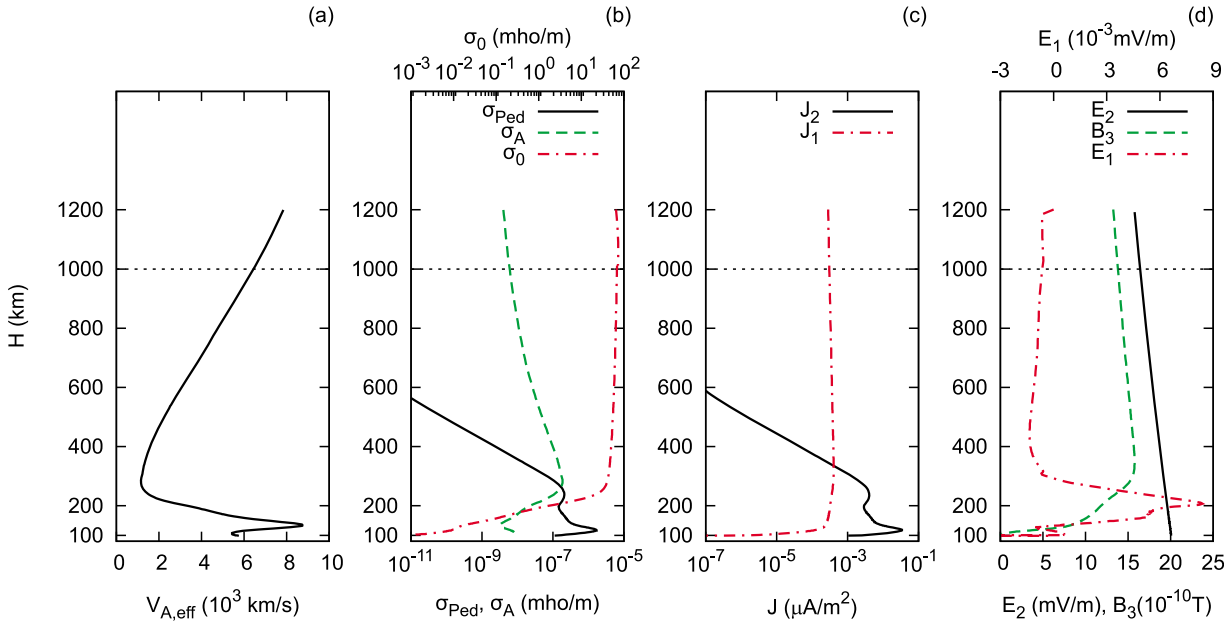

Figure 3. Initial profiles of the (a) effective Alfvén speed; (b) Pedersen, "Alfvén", and parallel conductivities; (c) transverse and parallel electric currents; and (d) electromagnetic field components. Everywhere, the vertical axis is the altitude. Horizontal dashed lines mark the top ionospheric boundary at 1000 km. The bottom boundary is at 100 km.

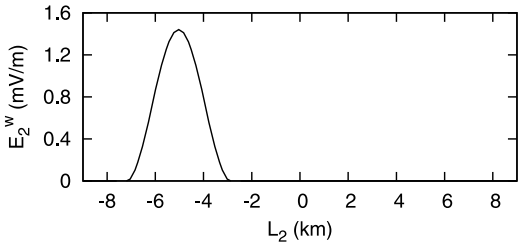

Figure 4. Transverse profile of the electric field of the Alfvén wave at $t = 1$ s at altitude 1105 km, the horizontal axis is the distance across the geomagnetic field calculated from the middle field line of the simulated area, positive direction of the horizontal axis is southward.

[S88, equations (69)–(72)], and excitation of fine structure of *O* [*Williams and McDonald*, 1987, equation (15)]. The electron temperature is found as $T_e = p_e/n_e$.

[33] The neutral gas components are immobile, the temperature T_n and the densities n_β of neutrals remain constant in time. Dynamic effects in the neutral gas due to coupling with ionospheric plasma, such as convection induced by ion drag, heating and upwelling, are omitted. These are reasonable assumptions because a typical duration of simulation with the present model is about one minute or less while changes in thermosphere occur on timescale of hours [*Wang et al.*, 2004].

3. Simulation of Interaction of an Alfvén Wave With the Ionosphere

[34] Previously, the interaction of a wave perturbation with the ionosphere was considered by *Zhu et al.* [2001]. The similarity between the simulation described below and the one of *Zhu et al.* [2001] is that in both simulations the perturbation is limited in transverse direction. The difference is that the perturbation in the present simulation is periodic in time while in *Zhu et al.* [2001] a constant perturbation is introduced at the top boundary at the start.

3.1. Simulation Parameters

[35] The simulation is carried out with the following parameters. The northern bottom corner of the simulation area (corner D in Figure B1) is at an altitude of 99.3 km, and a magnetic latitude of 71.641 degrees. The altitude of the northern top corner (*A* in Figure B1) is 1193.2 km. The distance between the bottom corners (*D* and *C* in Figure B1) is 14.49 km. The interface between the ionosphere and magnetosphere intersects the most northern geomagnetic field line (*AD* in Figure B1) at altitude of 1012 km. Resolution of the numerical grid (the mesh size) across the geomagnetic field varies from 161 m near the bottom end to 205 m near the top end. In the parallel direction, the grid resolution is about 799 m near the bottom and about 16.1 km near the top end.

[36] The grid parameters above are given for the central part *ABCD* of the main simulation area *A′B′C′D′* in Figure B1, where the transverse resolution is high and uniform. The detailed description of the numerical grid, including the role of side areas *A′ADD′* and *BB′C′C* with nonuniform transverse resolution, can be found in Appendix B.

[37] The convection electric field corresponds to $E_{conv} = 20$ mV/m at the bottom of the simulation domain and produces southward ion flow in the ionosphere. The initial equilibrium state of the system is shown in Figures 2 and 3. The ionospheric parameters used to start the process of calculation of the initial state (see Appendix C) correspond to the local time 6 am on January 1st, 1997, at a geomagnetic latitude of 72 degrees and a longitude of 336 degrees.

[38] In the simulation, an Alfvén wave with a period of 20 s is injected into the system through the top boundary. The wave amplitude and phase are specified in the equatorial plane (the boundary of the wave transport buffer) and the wave is transported (as a plane wave) along the geomagnetic field from the equatorial plane to the top boundary of the main simulation area, as discussed in Appendix A. Note, the wave transport buffer is introduced instead of a simple nonreflecting boundary condition used in *Sydorenko et al.* [2010] in order to account for non-periodic changes of the electromagnetic field. Wave propagation through the buffer is trivial, which is why it is only briefly described in the present paper. The Alfvén wave starts at the equatorial plane at time $t = -13.1$ s and it appears at the top boundary of the major simulation area at $t = 0.5$ s. In order to reduce the numerical cost, during the time interval from -13.1 s to 0 s only the electromagnetic field inside the wave transport buffer is advanced.

[39] The transverse profile of the electric field amplitude of the incident Alfvén wave is bell-shaped (proportional to $\cos^2[\pi(\xi_2 - \xi_2^*)/2\Delta]$ for $|\xi_2 - \xi_2^*| < \Delta$, where Δ is the width and ξ_2^* is the position of the maximum in dipole coordinates). In real space, the width of the profile at the equatorial plane is about 217 km while at the top of the simulation area it is about 4500 m (see Figure 4). The maximum amplitude of the incoming wave electric field in the equatorial plane is 0.6 mV/m. As the wave travels through the wave transport buffer, its amplitude increases due to convergence of the geomagnetic field. Reflection from the nonuniform Alfvén speed profile reduces amplitude of the wave reaching the bottom boundary of the buffer, but for the wave selected the reflection is weak, see Section 3.3. At the top boundary of the main simulation area, the maximum amplitude of the perturbation of the electric field is about 50 mV/m (see the solid red curve in Figure 6a). Note that this perturbation contains both the incident and the reflected waves.

3.2. Generation of Parallel Electric Fields and Emission of Alfvén Waves

[40] The parallel current of Alfvén waves is mostly closed by the Pedersen current within the E-layer, at altitudes between 105 km and 140 km, where the Pedersen conductivity (solid black curve in Figure 3b) maximizes (compare Figures 5b and 5e). Since the parallel conductivity σ_0 is low in the bottom of the ionosphere (see the dash-dot red curve in Figure 3b), intense parallel electric fields about 0.5 mV/m appear in order to support the parallel current (see Figure 5f). This electric field is electrostatic in nature and the charge separation producing it affects the transverse electric field as well (see Figure 5a for altitudes below 150 km). Joule heating by parallel electric fields is an important energy source for the electrons, which is demonstrated in Section 3.5. The wave creates significant plasma density (Figure 5c) and conductivity (Figure 5d) perturbations propagating across the

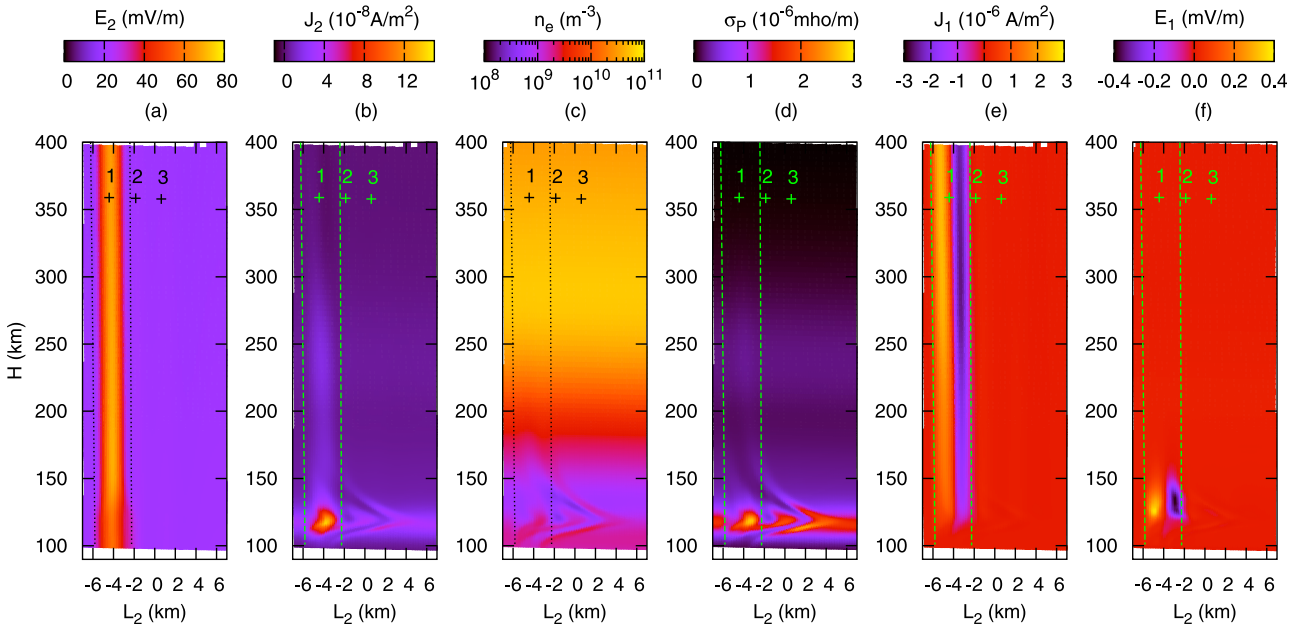

Figure 5. Two-dimensional color maps of the (a) transverse electric field, (b) transverse electric current, (c) electron number density, (d) Pedersen conductivity, (e) parallel electric current, and (f) parallel electric field at $t = 47.812$ s. Everywhere, the horizontal axis is the distance across the geomagnetic field calculated from the middle field line of the simulated area, positive direction of the horizontal axis is southward; the vertical axis is the altitude. Crosses 1, 2, and 3 mark probes where the time dependencies of electromagnetic fields shown in Figures 6a, 6b, and 6c are obtained. The vertical lines denote boundaries for the incoming Alfvén wave in case of wave propagation along the geomagnetic field only.

geomagnetic field with the background ion flow. The direction of propagation is defined by the existing convection electric field, which is southward in the present simulation. Of course, for northward convection electric field, the perturbations will be propagating northward. With time, these perturbations change their shape due to the velocity shear (compare the shape of perturbations in Figure 5d with the ion flow speed profiles in Figure 2e). Note that a similar distortion of the shape of the perturbation created by electron precipitation is reported in *de Boer et al.* [2010]. It is interesting that these perturbations induce parallel electric currents themselves, thus emitting Alfvén waves. This emission can be observed downstream of the incoming wave propagation channel (the channel is marked by vertical lines in Figure 5).

[41] Inside the incoming wave channel (in probe 1 in Figure 5), the phase shift between the electric and magnetic fields is small (compare solid red and dashed black curves in Figure 6a), which means that the reflection is weak and the incoming wave energy is mostly absorbed (the reflection coefficient is estimated below, in Section 3.3). Outside the channel (e.g. in probes 2 and 3 in Figure 5), the phase shift between perturbations of E_2 and B_3 is close to π (compare solid red and dashed black curves in Figure 6b for probe 2 or in Figure 6c for probe 3), which corresponds to the emission of Alfvén waves in the upward direction. Perturbations of the electromagnetic field in probe 2 are much weaker than the incoming wave (compare Figures 6a and 6b). The intensity of the emitted wave quickly decays with the distance from the incoming wave channel (compare the fields in probe 2 shown in Figure 6b with the fields in probe 3 shown in Figure 6c). One of the reasons for the emission decay is the aforementioned dispersion of the ionospheric density perturbation [which emits the wave] due to the velocity shear. Thus, for the wave and the ionosphere parameters selected in the present simulation, the emission of Alfvén waves by perturbations drifting in the ionosphere is a weak effect. The emission of Alfvén waves by ionospheric density perturbations in the presence of a background convection electric field has application in experiments on artificial heating of the ionosphere [e.g., *Kolesnikova et al.*, 2002; *Pokhotelov et al.*, 2004].

3.3. Wave Reflection

[42] Calculation of the reflection coefficient at the top boundary of the major simulation area is not straightforward because here the Alfvén speed changes rapidly with altitude (see Figure 3a). In this case, the classical dispersion relation of Alfvén waves, such as $\omega = \pm k_{||} V_{A,eff}$ for small transverse wave numbers, where $V_{A,eff} = (c^{-2} + V_A^{-2})^{-1/2}$ is the effective Alfvén speed, cannot be applied to separate the incoming and the outgoing waves. Below, the reflection coefficient is calculated at the equatorial boundary of the wave transport buffer (WTB). At the vicinity of this boundary, the Alfvén speed profile is almost flat (see Figure A1) and the Alfvén wave dispersion is classical. The reflection coefficient at the equatorial plane still characterizes well the reflection of the major simulation area because, first, there is no dissipation inside the WTB. And, second, reflection of the wave with period $T = 20$ s inside the WTB is minimal because its wavelength is much longer than the width of the Alfvén

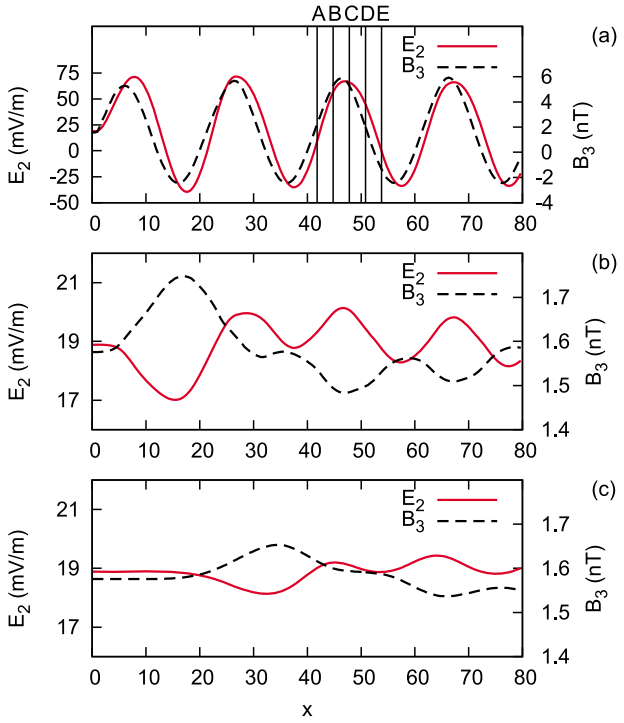

Figure 6. Time dependencies of components of the total transverse electric and magnetic fields obtained in probes shown in Figure 5. Figures 6a, 6b, and 6c are for probes 1, 2, and 3, respectively. In (a), the vertical lines A, B, C, D, and E denote times $t_A = 41.836$ s, $t_B = 44.824$ s, $t_C = 47.812$ s, $t_D = 50.8$ s, and $t_E = 53.788$ s, respectively, when the electron and ion temperature snapshots in Figures 8 and 9 are taken.

speed spike which has maximum at altitude 5920 km (see Figure A1).

[43] The power reflection coefficient for the simulated system is defined as

$$R_P = \frac{\int_T dt|P^-|}{\int_T dtP^+}, \tag{24}$$

where $P^{\pm}$ is the Poynting flux of the incoming (superscript +) and outgoing (superscript −) waves at the equatorial plane boundary of WTB, integration is over the wave period T. The denominator of (24) can be calculated directly as

$$\int_T dtP^+ = \int_T dt \int d\xi_2 d\xi_3 h_2 h_3 E_2^w B_3^w/\mu_0, \tag{25}$$

where all values at the RHS are taken in the equatorial plane $\xi_1 = 0$, the spatial integration is over the transverse cross section of the equatorial boundary of the WTB, E_2^w and B_3^w are the components of the *wave* electromagnetic field. It is important that in (25) the time integration interval ends *before* the first wave reflected from the ionosphere reaches the equatorial plane. Such time interval [−13.1 s : 6.9 s] is between the two dashed vertical lines in the left-hand side of Figure 7a.

[44] Once the reflected wave reaches the equatorial plane, the electromagnetic field there becomes a superposition of incoming and reflected waves: $E_2^w = E_2^+ + E_2^-$, $B_3^w = B_3^+ + B_3^-$, where superscripts + and − denote the incoming and the outgoing (reflected) waves. For Alfvén waves with classical dispersion one has $E_2^{\pm} = \pm V^* B_3^{\pm}$, where for small transverse wave numbers $V^* = V_{A,eff}$. The exact value of V^* is not important here. It is important, however, that both the incoming and the outgoing waves have the same V^*. Then

$$E_2^w B_3^w \equiv \left(E_2^+ + E_2^-\right)\left(B_3^+ + B_3^-\right) = E_2^+ B_3^+ + E_2^- B_3^-,$$

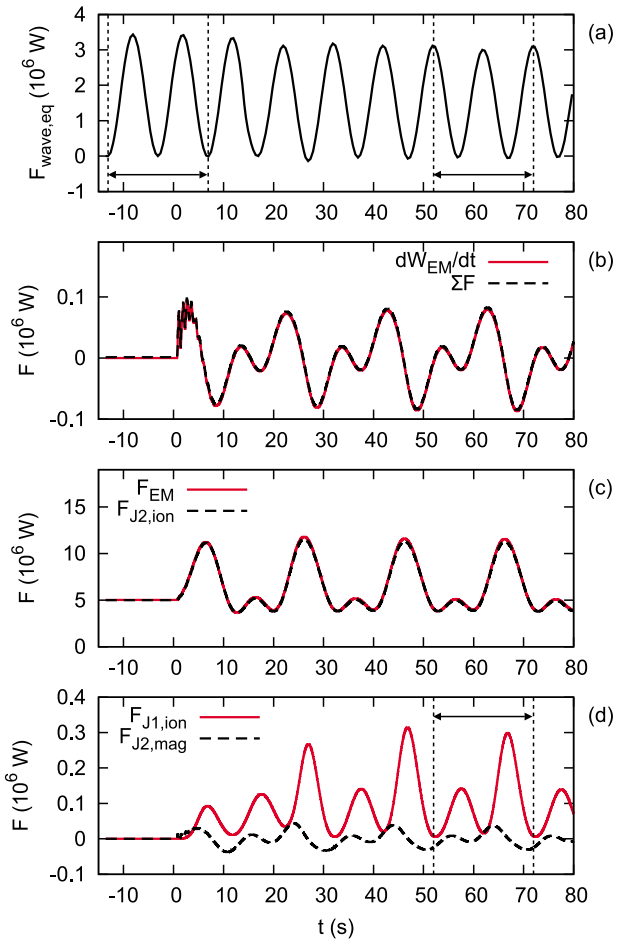

Figure 7. Time dependencies of the following parameters. (a) The wave electromagnetic energy flux through the equatorial boundary of the wave transport buffer area. (b) The LHS (solid red curve) and the RHS (dashed black curve) of the energy conservation law (27). (c) The total electromagnetic field energy flux through the top boundary (solid red curve), and the power spent on transverse plasma motion in the ionosphere (dashed black curve). (d) The power spent on parallel electron motion in the ionosphere (solid red curve) and the power spent on transverse plasma motion in the magnetospheric area (dashed black curve). The vertical lines and arrows in Figures 6a and 6d denote time intervals [−13.1 s : 6.9 s] and [52 s : 72 s] used for integration of the wave Poynting fluxes in Section 3.3 and energy losses due to the wave plasma motion in Sections 3.4.

and the numerator of (24) is calculated as

$$\int_T dtP^- = \int_T dt \int d\xi_2 d\xi_3 h_2 h_3 E_2^w B_3^w/\mu_0 - \int_T dtP^+. \quad (26)$$

In the first term in the RHS of (26), all values are in the equatorial plane $\xi_1 = 0$, the spatial integration is over the transverse cross section of the equatorial boundary of the WTB. The time integration interval in this term must start *well after* the first wave reflected from the ionosphere reaches the equatorial plane in order to exclude transient effects accompanying reflection of the very first wave period. Such time interval [52 s : 72 s] is between two dashed vertical lines in the right-hand side of Figure 7a. The last term in the RHS of (26) is calculated with (25).

[45] The wave Poynting flux $\int d\xi_2 d\xi_3 h_2 h_3 E_2^w B_3^w/\mu_0$ as a function of time which is used in (25) and (26), is shown in Figure 7a. Integration of this flux over the time interval [−13.1 s : 6.9 s] gives $\int_T dtP^+ = 3.418 \cdot 10^7$ J, whereas integration over the time interval [52 s : 72 s] gives the value of $3.02 \cdot 10^7$ J. Substituting these values into (26) gives $\int_T dtP^- = (3.02 - 3.418) \cdot 10^7$ J $= -0.398 \cdot 10^7$ J. Then, according to (24), the power reflection coefficient is $R_P = 0.398/3.418 = 0.116$. Thus, here the reflection is weak and most of the wave energy is absorbed in the ionosphere.

3.4. Energy Conservation

[46] The energy conservation in the simulated system is described by the Poynting theorem in the following form

$$\frac{\partial}{\partial t} \int_{V_{mag}+V_{ion}} \left[\frac{\varepsilon_0 \left(E_1^2 + E_2^2\right)}{2} + \frac{B_3^2}{2\mu_0} \right] d^3r = \int_S \frac{E_2 B_3}{\mu_0} ds - \int_{V_{mag}} E_1 J_1 d^3r - \int_{V_{ion}} E_1 J_1 d^3r - \int_{V_{mag}} E_2 J_2 d^3r - \int_{V_{ion}} E_2 J_2 d^3r, \quad (27)$$

where the integration of the electromagnetic energy density in the left-hand side (LHS) is over volumes of both the magnetospheric V_{mag} and ionospheric V_{ion} simulation areas (ABCD in Figure B1), and the surface integration of the Poynting vector (first term in the RHS) is over the top boundary (AB in Figure B1). Note that the first term in the RHS of equation (27) is positive if the Poynting vector is directed into the simulation area ($E_2 B_3 > 0$), and negative if the Poynting vector is directed outward ($E_2 B_3 < 0$). The electromagnetic energy flux through the field-line boundaries (AD and BC in Figure B1) is found to be very small and can be omitted. The flux through the bottom boundary (CD in Figure B1) is zero. The second and the third terms in the RHS of (27) describe the power spent by the electromagnetic field to support parallel plasma flows in the magnetospheric and ionospheric areas, respectively. The fourth and the fifth terms in the RHS of (27) describe the power spent by the electromagnetic field to support transverse plasma flows in the magnetospheric and ionospheric areas, respectively.

[47] Energy balance (27) is maintained well during the simulation; the LHS and the RHS of (27) are very close in value (compare the solid red and the dashed black curves in Figure 7b). For the selected parameters, the major terms in the RHS of (27) are the electromagnetic energy flux (solid red curve in Figure 7c) and the power spent on transverse plasma motion in the ionosphere (dashed black curve in Figure 7c). These two terms largely balance each other. The contribution of the energy losses due to transverse plasma motion in the magnetosphere (dashed black curve in Figure 7d) and due to parallel plasma motion in the ionosphere (solid red curve in Figure 7d) is about a few percent. The power spent on parallel plasma flows in the magnetospheric area is negligible.

[48] Terms in the RHS of (27) include both the background and the wavefields and electric currents. It is instructive to separate energy losses related with wave plasma motion only. To do this, the wave electric fields and currents must be calculated as

$$E_{1,2}^w = E_{1,2} - \langle E_{1,2} \rangle_T,$$
$$J_{1,2}^w = J_{1,2} - \langle J_{1,2} \rangle_T,$$

where $\langle\rangle_T$ denotes time averaging over the wave period T. Then the energy spent on the parallel or transverse wave plasma motion during one wave period is

$$W_{1,2}^w = \int_T dt \int_{V_{ion}+V_{mag}} E_{1,2}^w J_{1,2}^w d^3r, \quad (28)$$

where the time integration is over the wave period. Equation (28) with integration over time interval [52 s : 72 s] shown in Figure 7d gives the energy losses due to the parallel wave plasma motion $W_1^w = 0.213 \cdot 10^7$ J and the energy losses due to the transverse wave plasma motion $W_2^w = 2.794 \cdot 10^7$ J. Note that the sum of these values, $W_1^w + W_2^w = 3.007 \cdot 10^7$ J, is very close to the wave energy deposited in the ionosphere during one wave period, $3.02 \cdot 10^7$ J, calculated independently in the end of Section 3.3. This confirms the energy conservation in the simulation.

[49] Comparison of W_1^w and W_2^w shows that for the selected parameters of the wave and the ionosphere almost 93% of the energy lost by the Alfvén wave is expended in driving transverse flows of ionospheric ions, while only 7% is spent on parallel electron flows. This ratio should shift in favor of parallel flows in the case of waves with larger transverse wave numbers, which may be the reason for enhanced absorption of such waves in the ionosphere predicted by *Lessard and Knudsen* [2001]. The effect of the transverse wave number on the wave reflection will be discussed in a future publication.

3.5. Electron and Ion Heating

[50] Below, the electron and the ion heating and cooling terms affected by MI-coupling are discussed in order to verify correctness of the plasma heating model. Only high-level conclusions are given due to limited space. More technical details can be found in the auxiliary material.[1]

[51] As shown in Figure 8, Alfvén wave activity in the simulation causes intense oscillations of electron temperature in the ionosphere below 200 km. The two patches of relatively hot electrons in this figure coincide with the

[1] Auxiliary materials are available in the HTML. doi:10.1029/2012JA017693.

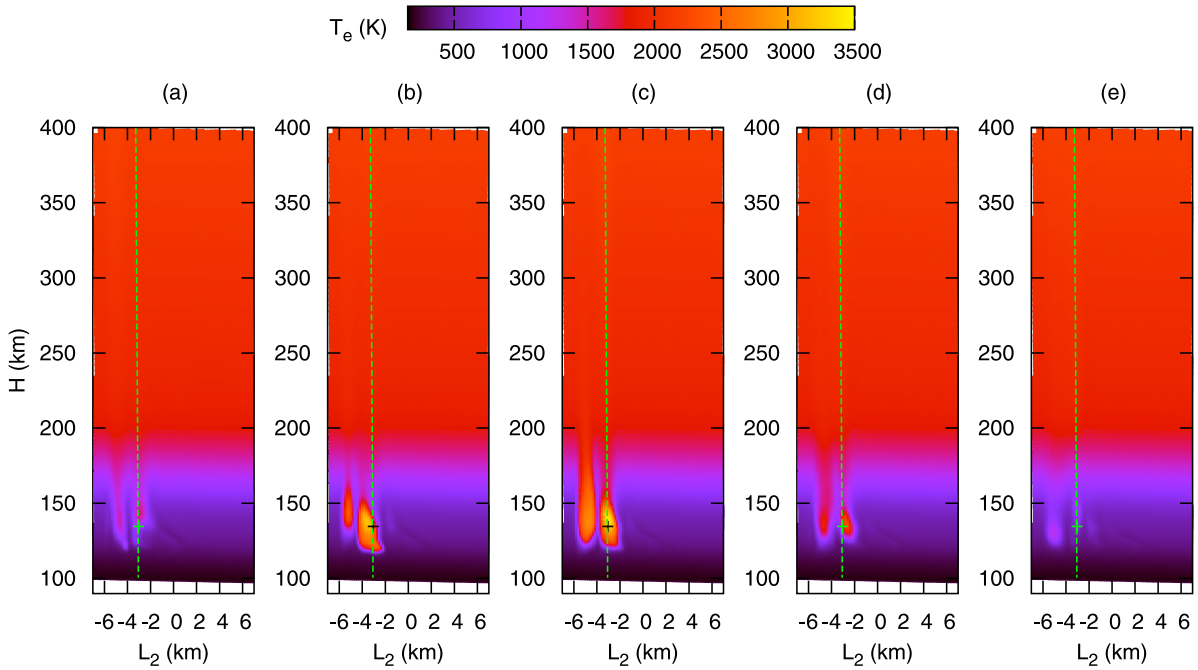

Figure 8. (a–e) Two-dimensional color maps of the electron temperature obtained at times t_A, t_B, t_C, t_D, and t_E respectively (the times are defined in Figure 6a). Everywhere, the horizontal axis is the distance across the geomagnetic field calculated from the midplane of the simulation area, positive direction of the horizontal axis is southward, the vertical axis is the altitude. The green dashed vertical line marks the geomagnetic field line used for the analysis of relative importance of different electron heating and cooling terms in Section 3.5. The actual profiles of these terms are given in the auxiliary material. The cross marks position of the probe where time dependencies discussed in the auxiliary material are obtained.

location of intense parallel electric currents and fields (compare Figure 8c with Figures 5e and 5f). Analysis of different terms in the RHS of (23) reveals that the major electron heating mechanism in the lower ionosphere, below 160 km, is frictional heating due to parallel electron flows. Above 160 km, the divergence of the thermal conductivity heat flow is a significant heating source. Cooling due to inelastic collisions with neutrals is the dominant electron energy sink term everywhere in the simulated system. Terms associated with convection ($\propto u_{e,1}\,\partial p_e/\partial\xi_1$) and compression ($\propto p_e\partial(u_{e,1}h_2h_3)/\partial\xi_1$) in (23) are important above 160 km, though usually they tend to cancel each other. Electron cooling due to heat exchange with ions is of some importance for altitudes above 325 km.

[52] Alfvén waves perform intense ion heating as well. In Figure 9, the area of increased ion temperature is stretched along the middle of the wave propagation channel, where the transverse electric field is maximal (compare Figure 9c and Figure 5a). The major ion heating process is ion flow friction with neutral gas. The major ion cooling process is heat exchange with neutrals. Above 250 km, heat exchange with electrons becomes another noticeable heating source. The convection ($\propto u_{\alpha,2}\,\partial p_\alpha/\partial\xi_2$) and compression ($\propto p_\alpha\partial(u_{\alpha,2}h_1h_3)/\partial\xi_2$) terms in (18) are relatively minor. Below 200 km, ion frictional heating and ion-neutral heat exchange virtually balance each other, and the ion temperature oscillates approximately as $T_i \propto E_2^2$. At higher altitudes, above 300 km, there is no *instantaneous* balance between major heating and cooling terms, and the ion temperature gradually rises until the balance between the *time-averaged* values of the ion-neutral heat exchange term, the frictional term, and the electron-ion heat exchange term is achieved.

[53] The evolution of the electron and ion temperature in space and time and the importance of different heating and cooling processes described above agrees qualitatively with *Zhu et al.* [2001].

4. Conclusion

[54] An advanced two-dimensional multifluid model of the coupled magnetosphere and ionosphere is developed on the basis of *Schunk* [1988] and *Sydorenko et al.* [2010]. A representative simulation is performed where the quasi-equilibrium ionosphere with externally applied transverse convection electric field is perturbed by a shear Alfvén wave. The major purpose of this simulation is validation and justification of the new model. The simulation reproduces the following physical effects.

[55] When the wave current closes through the highly collisional plasma of the E-layer, strong parallel electric fields of the order of 0.5 mV/m are formed in order to support Alfvén wave parallel currents with amplitude about 1 μA/m^2. The parallel electron flow is stable with respect to drift instability [*Jackson*, 1960] because the electron flow speed (about 20 km/s) is much smaller than the electron thermal speed (about 200 km/s). The wave also creates intense density perturbations which convert transverse convection currents into field-aligned currents. Thus, the

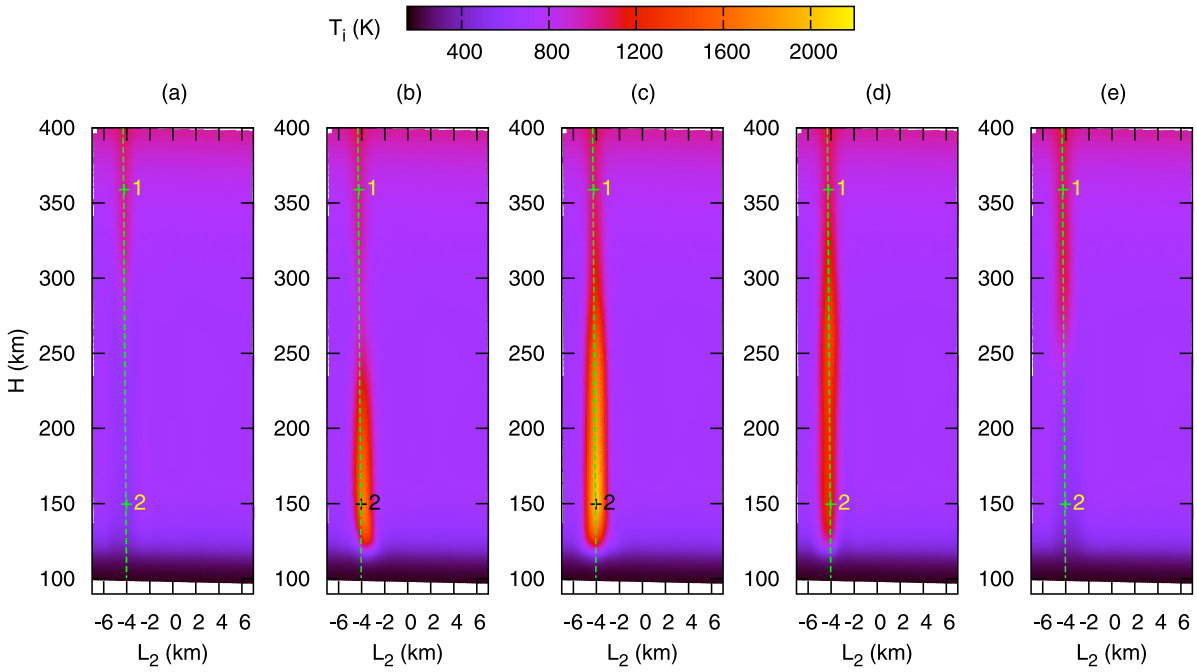

Figure 9. (a–e) Two-dimensional color maps of the ion temperature obtained at times t_A, t_B, t_C, t_D, and t_E respectively (the times are defined in Figure 6a). Everywhere, the horizontal axis is the distance across the geomagnetic field calculated from the midplane of the simulation area, positive direction of the horizontal axis is southward, the vertical axis is the altitude. The green dashed vertical line marks the geomagnetic field line used for the analysis of relative importance of different ion heating and cooling terms in Section 3.5. The actual profiles of these terms are given in the auxiliary material. Crosses 1 and 2 mark positions of probes where time dependencies discussed in the auxiliary material are obtained.

perturbations emit Alfvén waves themselves, though the intensity of this emission is weak for the range of parameters selected. The currents and the emission may be stronger for waves with shorter transverse wavelength, but the density perturbations disperse with time due to shear of the transverse ion flow inside the E-layer [*de Boer et al.*, 2010]. This effect may be more significant for such narrow waves.

[56] In the present simulation, the reflection is weak and about 88.4% of the energy flux of the incident wave is absorbed. The transverse wavelength of 4.5 km is too large to attribute such strong absorption to the effect of short transverse wavelength predicted by *Lessard and Knudsen* [2001]. Most of the absorbed energy, about 93%, goes into transverse ion flows, while the 7% remaining is spent to support parallel electric currents. This indicates that inside the E-layer the Pedersen conductivity is, on one hand, low enough to allow large amplitude of the wave transverse electric field, and, on the other hand, is sufficient to ensure that the Pedersen current is stronger than the wave polarization current and the related Joule losses are substantial.

[57] Plasma flows created by the absorbed wave energy cause large oscillations of electron and ion temperatures in the ionosphere. Electrons are heated by the parallel currents at the lower part of the ionosphere, where the parallel electric field is the strongest. Ions are heated by the transverse ion currents induced by the wave. The major cooling processes are inelastic collisions between electrons and neutrals and resonant and non-resonant collisions between ions and neutrals. Important factors affecting the electron temperature at higher altitudes (above 160 km in the present simulation) are the thermal conductivity, compression or rarefaction, and convection. The energy exchange between electrons and ions due to Coulomb collisions is important above 250–300 km.

[58] The model described still has room for improvement. A realistic ionosphere was added as an extension to the previously developed model of the ionospheric Alfvén resonator. Shear Alfvén waves in the IAR create parallel electric currents while compressional Alfvén waves do not. For this reason, the compressional Alfvén wave and the Hall effects are not included in the present model. This is a drawback, however, because in the E-layer the Hall and the Pedersen conductivities are comparable with each other. Possible effects of the Hall currents in the ionosphere include rotation of the magnetic field of the Alfvén wave [*Hughes*, 1974], non-zero magnetic field perturbation below the ionosphere [*Lysak*, 1999], excitation of compressional Alfvén waves propagating across the geomagnetic field. The latter will be an additional energy loss channel of the shear Alfvén wave [*Lysak*, 1997]. Next, the equations are written in the frame moving with the neutral flow. Thus, it is assumed that the direction and the speed of the neutral wind does not change with altitude, while in fact there may be a significant altitude shear of the neutral wind [*Rees et al.*, 1976]. This will affect the electric field and the absorption of the wave. Another significant simplification is the assumption that the ions in the ionosphere move across the geomagnetic field only. Thus the model misses formation of ion outflows [*Yau et al.*, 2007] as

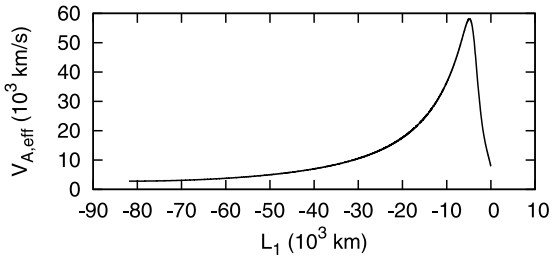

Figure A1. Profile of the effective Alfvén speed along the middle geomagnetic field line in the wave transport buffer area where equation (A3) are solved. The horizontal axis is the distance along the field line calculated from the top boundary of the major simulation area ($L_1 = 0$), the positive direction of the axis is toward the Earth. The buffer area is for $L_1 < 0$, the equatorial plane is at $L_1 = -81891$ km, the main simulation area is for $L_1 > 0$ (the effective Alfvén speed profile in the main simulation area is in Figure 3a).

well as excitation of ion-acoustic waves in the ionosphere explaining radar observations of naturally enhanced ion acoustic lines [*Sedgemore-Schulthess and St.-Maurice*, 2001]. A valuable addition would be neutral species dynamics and heating, which will allow to study outflows of neutrals [*Wang et al.*, 2004].

[59] Although the model is not fully comprehensive, it does capture important physical processes accompanying interaction of shear Alfvén waves with the ionosphere. Thermal effects described above are in qualitative agreement with the results of *Rees et al.* [1971], *Noël et al.* [2000], *Zhu et al.* [2001], and *de Boer et al.* [2010]. A distinctive feature of the present model is that it combines a realistic ionosphere with a magnetospheric component which can extend for thousands of kilometers along the geomagnetic field above the ionosphere. This allows for future studies of feedback effects in the ionospheric Alfvén resonator [*Lysak*, 1991]. Note that in the present paper, the magnetospheric area is only about 200 km long because the focus is on the validity of the ionospheric model and the wave absorption. It is necessary to mention that in addition to Alfvén wave dynamics, the model includes chemical reactions between ionospheric ions and neutrals, as well as ionization and heating of plasma by auroral electron precipitation. These properties are turned off in the model results presented, and will be described in a future publication.

Appendix A: Boundary Conditions

[60] At the northern $\xi_{2,\min}$ ($A'D'$ in Figure B1) and southern $\xi_{2,\max}$ ($B'C'$ in Figure B1) boundaries, the parallel electric field, ion densities, ion and electron pressures and parallel velocities are equal to the values set as the initial state.

[61] The simulated system is azimuthally symmetric and azimuthal currents are omitted. In stationary state, currents in the ionosphere and magnetosphere create a purely azimuthal magnetic field, which is zero below the ionosphere. For a shear Alfvén wave, *Hughes* [1974] demonstrated that its magnetic perturbation is almost completely screened by the ionosphere (such a wave is referred to as Part 2 in *Hughes* [1974]). Thus, the boundary condition for the magnetic field at the bottom of the ionospheric layer $\xi_{1,\max}$ ($D'C'$ in Figure B1) is

$$B_3\left(\xi_{1,\max}\right) = 0. \tag{A1}$$

Also, here $J_1(\xi_{1,\max}) = 0$, $n_\alpha(\xi_{1,\max}) = 0$, and $p_e(\xi_{1,\max}) = 0$.

[62] At the top end $\xi_{1,\min}$ ($A'B'$ in Figure B1), the electromagnetic field is represented as a superposition of the initial field and the perturbation fields B_3^w and E_2^w:

$$\begin{aligned} B_3\left(\xi_{1,\min},\xi_2,t\right) &= B_3\left(\xi_{1,\min},\xi_2,0\right) + B_3^w\left(\xi_{1,\min},\xi_2,t\right),\\ E_2\left(\xi_{1,\min},\xi_2,t\right) &= E_2\left(\xi_{1,\min},\xi_2,0\right) + E_2^w\left(\xi_{1,\min},\xi_2,t\right). \end{aligned} \tag{A2}$$

Maxwell's equations for the perturbation fields can be transformed as follows:

$$\begin{aligned} &\left(\frac{\partial}{\partial t} \pm \frac{V_{A,eff}}{h_1}\frac{\partial}{\partial \xi_1}\right)\left(E_2^w \pm V_{A,eff}B_3^w\right)\\ &\quad = B_3^w\left(\frac{V_{A,eff}}{h_1}\frac{\partial V_{A,eff}}{\partial \xi_1} - \frac{V_{A,eff}^2}{2h_1h_3^2}\frac{\partial h_3^2}{\partial \xi_1}\right) \mp E_2^w\frac{V_{A,eff}}{2h_1h_2^2}\frac{\partial h_2^2}{\partial \xi_1}. \end{aligned} \tag{A3}$$

At each time step, equation (A3) are solved using a semi-Lagrangian method [*Staniforth and Cote*, 1991] in a buffer area stretching from the equatorial plane $\xi_1 = 0$ to the top end of the main simulation area $\xi_{1,\min}$ (the buffer is shown as the white box in Figure 1). The required boundary conditions are

$$\begin{aligned} F^+(0,\xi_2,t^n) &= 2E_2^+ f_1(\xi_2) f_2(t^n),\\ F^-\left(\xi_{1,\min}^+,\xi_2,t^n\right) &= \left(E_2^w - V_{A,eff}B_3^w\right)\left(\xi_{1,\min}^+,\xi_2,t^n\right), \end{aligned} \tag{A4}$$

where $F^\pm = E_2^w \pm V_{A,eff}B_3^w$ are the incoming (+) and the outgoing (−) Alfvén wave characteristics, E_2^+ is the amplitude of the electric field of incoming Alfvén wave at the equatorial plane, $f_1(\xi_2)$ is a shape function describing the transverse profile of the wave, $f_2(t)$ describes variation of this field with time, $|f_{1,2}| \le 1$, and $\xi_{1,\min}^+$ is the coordinate of the node inside the major simulation area adjacent to the boundary $\xi_{1,\min}$. Note that (A4) is applied at time t^{n+1}, when the electromagnetic fields at time t^n in the RHS of (A4) are already known. Once the updated $F^\pm(\xi_{1,\min}, \xi_2, t^{n+1})$ are calculated, the updated magnetic field perturbation at the top boundary is

$$B_3^w\left(\xi_{1,\min},\xi_2,t^{n+1}\right) = \left(\frac{F^+ - F^-}{2V_{A,eff}}\right)\left(\xi_{1,\min},\xi_2,t^{n+1}\right),$$

and the total updated magnetic field at the top end boundary is calculated using (A2).

[63] The Alfvén speed profile in the buffer area shown in Figure A1 is calculated using the same density profile functions of H^+ and O^+ ions as the ones used in the magnetospheric part of the main simulation area. The Alfvén speed profile is continuous across the top side boundary of the main simulation area. Inside the buffer area, the Alfvén speed does not change in time.

[64] The procedure of transporting the Alfvén wave characteristics through the buffer area is relatively inexpensive numerically and provides more accurate values of B_3^w at the top boundary than a simplified version of (A3) with zero

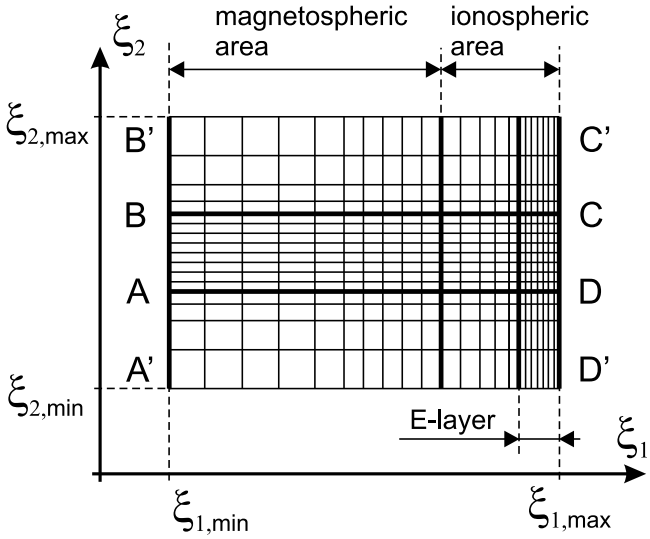

Figure B1. Schematic of the numerical grid in dipole coordinates. Here $A'B'$ and $C'D'$ are the high-altitude and the low-altitude borders, $A'D'$ and $B'C'$ are the northern and the southern borders (geomagnetic field lines). Only values from the middle area $ABCD$ are considered in the present paper.

RHS used in *Sydorenko et al.* [2010]. In particular, the new boundary condition ensures that when an Alfvén wave moves away from the boundary, the electromagnetic field at the boundary is defined mostly by local charge separation and currents rather than by the wave.

Appendix B: Computational Grid

[65] Electromagnetic field components E_1, E_2, and B_3 are defined on separate staggered grids in dipole coordinates. Each grid is structured, rectangular, and nonuniform. A qualitative schematic of one of these grids is shown in Figure B1.

[66] The parallel grid resolution is maximal near the bottom of the ionosphere (in the E-layer), where vertical shear of transverse ion flow velocity is strong and small scale structures are most likely to occur. Above the E-layer, the parallel grid resolution decreases. In the present simulation, the size of the grid cell in the parallel direction changes with altitude as shown in Figure B2.

[67] The transverse grid resolution is maximal and constant in the middle section (rectangle $ABCD$ in Figure B1) of the simulation area. In areas adjacent to the middle section from the northern and southern sides (rectangles $A'ADD'$ and $BB'C'C$ in Figure B1), the transverse grid size gradually increases as one approaches to the borders $A'D'$ or $B'C'$, respectively. Note that boundary conditions at $A'D'$ and $B'C'$ assume that the plasma is unperturbed. The role of the nonuniform sections $A'ADD'$ and $BB'C'C$ is (i) to prevent perturbations created in the middle section (and drifting with the ion flow) from reaching boundaries $A'D'$ and $B'C'$ and (ii) to do it at a minimal numerical cost. In the present simulation, the transverse width of sections $A'ADD'$ and $BB'C'C$ near the bottom end is $L_{D'D} \approx L_{CC'} \approx 9.7$ km (compare with $L_{DC} \approx 14.5$ km). Each of these sections contains 11 cells in the transverse direction (for comparison, the central segment DC contains 90 cells), at the bottom boundary the minimal cell width is 186 m, the maximal cell width is 2237 m.

[68] It is necessary to mention that inside the transversely nonuniform sections, the transverse advection of densities and pressures using the semi-Lagrangian method becomes strongly diffusive. Because of this, only values from the middle area $ABCD$ are considered as a valid simulation output. Also, the intensity of the incoming Alfvén wave is nonzero only inside the uniform part AB of the high altitude border $A'B'$.

Appendix C: Initial State

[69] The initial state is calculated in two stages. At the first stage, the densities and temperatures inside the ionosphere are obtained from the IRI 2007 model (IRI, International reference ionosphere, 2007, http://nssdcftp.gsfc.nasa.gov/models/ionospheric/iri/iri2007/) for ions ($n_{\alpha,0}$, $T_{i,0}$) and electrons ($T_{e,0}$), and from MSIS86 model (A. E. Hedin, Mass-spectrometer-incoherent-scatter (MSIS) neutral atmosphere model, 1987, http://nssdcftp.gsfc.nasa.gov/models/atmospheric/msis/msis86/) for neutrals ($n_{\beta,0}$, T_n). Profiles of H^+ and O^+ ion densities in the magnetospheric region are taken from [*Sydorenko et al.*, 2010] and scaled in order to ensure continuity of densities across the ionosphere-magnetosphere interface. For the same purpose, density profiles of ionospheric ions N^+, N_2^+, NO^+, and O_2^+ are multiplied by a shape function which equals to 1 below 780 km and 0 above 940 km, and monotonically decreases (as $\sin^2$) between these altitudes. Note that these ions are minor at such high altitudes. Only N^+ density (green dashed curve in Figure 2b) is noticeable near the interface, but it is only about 10% of the H^+ density before applying the shape function. Temperatures of H^+, O^+, and e^- in the magnetospheric region are calculated as described in *Sydorenko et al.* [2010], with values at the ionosphere-magnetosphere interface equal to the ion and electron ionospheric temperatures, respectively. The transverse electric field along the low-altitude boundary of the ionosphere $\xi_{1,\max}$ is set equal to a constant value,

$$E_{2,0}(\xi_{1,\max}, \xi_2) = E_{conv},$$

where E_{conv} is the input parameter describing the convection electric field. Inside the simulated area, the initial transverse electric field $E_{2,0}$ satisfies

$$\frac{\partial h_2 E_{2,0}}{\partial \xi_1} = 0.$$

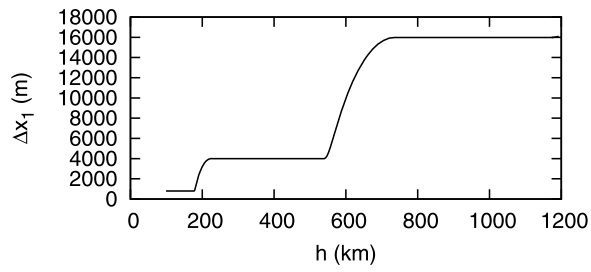

Figure B2. Dependence of the size of the grid cell in the parallel direction on altitude.

Each ion species produces the following transverse electric current in the ionosphere $J_{\alpha,2,0} = \sigma_{P\alpha} E_{2,0}$, which allows to specify the transverse ion velocity $u_{\alpha,2,0} = J_{\alpha,2,0}/en_{\alpha,0}$. The magnetic field is calculated from

$$\frac{1}{h_1 h_3}\frac{\partial h_3 B_3}{\partial \xi_1} = -\mu_0 \sum_{\alpha} J_{\alpha,2,0}.$$

with boundary condition (A1). The parallel electric current is calculated using (4), then the parallel electron velocity is calculated as $v_{e,1} = -J_1/en_e$, and the parallel electric field is found with equations (3a) and (3b) where $\partial J_1/\partial t = 0$ and $\partial n_\alpha/\partial t = 0$.

[70] The temperatures provided by the IRI 2007 model do not balance the RHS of the pressure equations (18) and (23), which is why the system state obtained at the first stage is not stationary. At the second stage, a fully self-consistent simulation of the system is performed without any external perturbations until the rates of change of plasma parameters decrease everywhere significantly. For the simulation described in the present paper, this stage lasts for 120 s. The new stationary state is saved as an input file for future use. It is necessary to mention that a few cell rows along the northern and southern boundaries must be discarded because they contain strong transverse non-uniformities.

[71] **Acknowledgments.** The present study was supported by the Canadian Space Agency (CSA) and the National Sciences and Engineering Research Council of Canada (NSERC).

[72] Robert Lysak thanks Jean-Pierre St. Maurice and another reviewer for their assistance in evaluating this paper.

References

de Boer, J. D., J.-M. A. Noël, and J.-P. St.-Maurice (2010), The effects of mesoscale regions of precipitation on the ionospheric dynamics, electrodynamics and electron density in the presence of strong ambient electric fields, *Ann. Geophys.*, *28*, 1345–1360.

Hughes, W. J. (1974), The effect of the atmosphere and ionosphere on long period magnetospheric micropulsations, *Planet. Space Sci.*, *22*, 1157–1172.

Jackson, E. A. (1960), Drift instabilities in a Maxwellian plasma, *Phys. Fluids*, *3*(5), 786–792.

Kirchengast, G. (1996), The Graz ionospheric flux tube simulation model, in *Solar-Terrestrial Energy Program: Handbook of Ionospheric Models*, edited by R. W. Schunk, pp. 73–94, Utah State Univ., Logan.

Kolesnikova, E., T. R. Robinson, J. A. Davies, D. M. Wright, and M. Lester (2002), Excitation of Alfvén waves by modulated HF heating of the ionosphere, with application to fast observations, *Ann. Geophys.*, *20*, 57–67.

Lessard, M. R., and D. J. Knudsen (2001), Ionospheric reflection of small-scale Alfvén waves, *Geophys. Res. Lett.*, *28*(18), 3573–3576.

Lysak, R. L. (1991), Feedback instability of the ionospheric resonant cavity, *J. Geophys. Res.*, *96*, 1553–1568.

Lysak, R. L. (1997), Propagation of Alfvén waves through the ionosphere, *Phys. Chem. Earth*, *22*(7–8), 757–766.

Lysak, R. L. (1999), Propagation of Alfvén waves through the ionosphere: Dependence on ionospheric parameters, *J. Geophys. Res.*, *104*(A5), 10,017–10,030.

Noël, J.-M. A., J.-P. St.-Maurice, and P.-L. Blelly (2000), Nonlinear model of short-scale electrodynamics in the auroral ionosphere, *Ann. Geophys.*, *18*, 1128–1144.

Noël, J.-M. A., J.-P. St.-Maurice, and P.-L. Blelly (2005), The effect of E-region wave heating on electrodynamic structures, *Ann. Geophys.*, *23*, 2081–2094.

Pokhotelov, D., W. Lotko, and A. V. Streltsov (2004), Simulations of resonant Alfvén waves generated by artificial HF heating of the auroral ionosphere, *Ann. Geophys.*, *22*, 2943–2949.

Rees, D., E. B. Dorling, K. H. Lloyd, and C. Low (1976), The role of neutral winds and ionospheric electric field in forming stable sporadic E-layers, *Planet. Space Sci.*, *24*, 475–478.

Rees, M. H., R. A. Jones, and J. C. G. Walker (1971), The influence of field-aligned currents on auroral electron temperatures, *Planet. Space Sci.*, *19*, 313–325.

Schunk, R. W. (1988), A mathematical model of the middle and high latitude ionosphere, *Pure Appl. Geophys.*, *127*, 255–303.

Schunk, R. W. (Ed.) (1996), *Solar-Terrestrial Energy Program: Handbook of Ionospheric Models*, Utah State Univ., Logan.

Sedgemore-Schulthess, F., and J.-P. St.-Maurice (2001), Naturally enhanced ion-acoustic spectra and their interpretation, *Surv. Geophys.*, *22*, 55–92.

Staniforth, A., and J. Cote (1991), Semi-Lagrangian integration schemes for atmospheric models–a review, *Mon. Weather Rev.*, *119*, 2206–2223.

Streltsov, A. V., and W. Lotko (2004), Multiscale electrodynamics of the ionosphere-magnetosphere system, *J. Geophys. Res.*, *109*, A09214, doi:10.1029/2004JA010457.

Sydorenko, D., R. Rankin, and K. Kabin (2010), Excitation and steepening of ion-acoustic waves in the ionospheric Alfvén resonator, *J. Geophys. Res.*, *115*, A11212, doi:10.1029/2010JA015448.

Wang, W., M. Wiltberger, A. G. Burns, S. C. Solomon, T. L. Killeen, N. Maruyama, and J. G. Lyon (2004), Initial results from the coupled magnetosphere-ionosphere-thermosphere model: thermosphere-ionosphere responses, *J. Atmos. Sol. Terr. Phys.*, *66*, 1425–1441.

Williams, P. J. S., and J. N. McDonald (1987), Electron temperature and electron density in the F-region of the ionosphere. II. The role of atomic oxygen and molecular nitrogen, *J. Atmos. Terr. Phys.*, *49*, 873–877.

Yau, A. W., T. Abe, and W. K. Peterson (2007), The polar wind: Recent observations, *J. Atmos. Sol. Terr. Phys.*, *69*, 1936–1983.

Young, D. M. (1970), Convergence properties of the symmetric and unsymmetric successive overrelaxation methods and related methods, *Math. Comput.*, *24*(112), 793–807.

Zhu, H., A. Otto, D. Lummerzheim, M. H. Rees, and B. S. Lanchester (2001), Ionosphere-magnetosphere simulation of small-scale structure and dynamics, *J. Geophys. Res.*, *106*, 1795–1806, doi:10.1029/1999JA000291.